Chemical Science

ROYAL SOCIETY OF CHEMISTRY

EDGE ARTICLE

View Article Online
View Journal | View Issue

Check for updates

Cite this: *Chem. Sci.*, 2026, **17**, 6956

All publication charges for this article have been paid for by the Royal Society of Chemistry

Open Access Article. Published on 22 1447. Downloaded on 10/12/47 07:47:25 .
This article is licensed under a Creative Commons Attribution 3.0 Unported Licence.

Atomic-level interface engineering enables efficient and durable acidic hydrogen evolution of osmium at large current densities

Qianyi Lin, Jun Yu,* Mansheng Liao, Weidong Liang, Yayun Hong, Huiqi Li, Zhongxin Song and Lei Zhang *

Received 11th December 2025
Accepted 9th February 2026

DOI: 10.1039/d5sc09741j

rsc.li/chemical-science

Osmium (Os), the least expensive member of the platinum-group metals, has emerged as a promising alternative to Pt-based catalysts for the hydrogen evolution reaction (HER). However, Os-based electrocatalysts still suffer from poor stability under acidic conditions, despite recent efforts to mitigate H* over-adsorption for improved intrinsic activity. Here, we design a porous CeO_2 support that enables the atomic dispersion of Os, forming an Os single-atom catalyst (Os_{SA}–CeO_2). Unlike traditional flat-film supports, the porous CeO_2 architecture prevents Os aggregation and achieves 100% interfacial anchoring of Os atoms. The resulting strong electronic coupling enables tight anchoring of Os and activates the CeO_2 matrix with abundant oxygen vacancies, which facilitate H_2O dissociation to sustainably supply protons for rapid consumption at large current densities. Also, the generated OH* species are adsorbed by the oxygen vacancies, thus preventing the Os sites from oxidative dissolution. As a result, Os_{SA}–CeO_2 exhibits over 500 h of durability at 100 mA cm^{-2} without performance decay—surpassing all previously reported Os-based HER catalysts. This work provides a general strategy for achieving complete interfacial anchoring of active metal atoms to enhance catalytic stability without sacrificing activity through support activation.

Introduction

The transition to sustainable and non-polluting energy sources has become increasingly urgent amid the global energy, environmental, and geopolitical crises. Among various clean energy technologies, "green hydrogen" has attracted particular attention as a zero-carbon fuel to play a dominant role in the future hydrogen economy.[1–4] Electrocatalytic water splitting powered by renewable energy sources (*e.g.*, solar and wind) represents one of the most promising routes for producing high-purity green hydrogen.[5–7] As the cost of renewable electricity continues to decline, the price, activity, and durability of electrocatalysts for the hydrogen evolution reaction (HER) are becoming the primary factors determining the overall economic feasibility of this process.[6,8–10]

Platinum (Pt)-based catalysts exhibit the highest HER activity due to their optimal hydrogen adsorption free energy. However, the high cost and scarcity of Pt significantly hinder their large-scale application.[6,11–13] Osmium (Os), the least expensive member of the platinum group metals (PGMs), has recently emerged as a potential alternative to Pt-based catalysts.[14–17] A fundamental challenge for Os-based HER catalysts is their tendency to over-adsorb hydrogen intermediates (H*), which results in inherently low HER activity.[18,19] To address this, several strategies have been developed to tune the electronic structure of Os and modulate its hydrogen adsorption behavior, such as supporting Os nanoparticles on TiO_2,[20] constructing heterostructures like Os–$OsSe_2$,[15,18,19] and introducing anion doping.[21] While these approaches have improved catalytic performance, achieving long-term stability, particularly at high current densities (≥100 mA cm^{-2}), remains a major challenge.[15,18,19]

The instability of Os-based catalysts primarily originates from nanoparticle aggregation *via* Ostwald ripening and the easily fluctuating valence states of Os under the harsh conditions of the HER.[14,22] At large current densities, oxidative dissolution of Os becomes more pronounced due to the rapid consumption of local H^+ and the accumulation of newly generated OH^- species derived from H_2O dissociation.[23] Anchoring Os onto reducible metal oxides, such as CeO_2, offers a promising pathway to enhance stability. The facile Ce^{4+}/Ce^{3+} redox cycling and high-order f orbitals of CeO_2 facilitate strong electronic coupling with supported metal atoms.[24–27] Moreover, the oxyphilic nature of Ce and the ease of oxygen vacancy formation endow CeO_2 with a strong affinity for OH^- species,[23,28–30] which can effectively suppress the adsorption of OH^- on Os and thus prevent its oxidative dissolution. To achieve these benefits, each Os atom must directly interact with neighboring Ce atoms *i.g.* achieving atomic dispersion of Os on CeO_2.[31–33] However, the fabrication of this precise architectural structure presents a great challenge and it requires the investigation of the thermodynamic stability properties of isolated Os atoms.

College of Chemistry and Environmental Engineering, Shenzhen University, Shenzhen 518071, China. E-mail: yujun@szu.edu.cn; lei.zhang@szu.edu.cn

© 2026 The Author(s). Published by the Royal Society of Chemistry

Open Access Article. Published on 22 1447. Downloaded on 10/12/47 07:47:25 .
This article is licensed under a Creative Commons Attribution 3.0 Unported Licence.

In this work, we first investigated the structural stability and hydrogen adsorption behavior of atomically dispersed Os on CeO_2 (Os_{SA}–CeO_2) using density functional theory (DFT) calculations. The results reveal that Os atoms can be strongly anchored within the CeO_2 lattice, while their excessive H* adsorption is effectively mitigated. Guided by these insights, we synthesized Os_{SA}–CeO_2 *via* a two-step electrodeposition method. A CeO_2 thin film was first deposited onto a conductive carbon fiber substrate, followed by O_2 annealing to create a porous structure that promotes atomic Os dispersion. This architecture introduces abundant oxygen vacancies and induces lattice compression, which shortens the distance between Os atoms and adjacent vacancies. These features facilitate H_2O dissociation and the subsequent migration of H* species to neighboring Os sites, providing a continuous hydrogen source for proton consumption at large current densities. Meanwhile, the generated OH* intermediates are preferentially adsorbed by the oxygen vacancies rather than the Os sites, effectively suppressing oxidative dissolution. Consequently, Os_{SA}–CeO_2 exhibits a remarkably low overpotential of 97 mV and over 500 h of durability at 100 mA cm^{-2} with negligible degradation, surpassing nearly all previously reported Os-based HER catalysts.

Results and discussion

DFT calculations for material design

To assess the feasibility of Os incorporation into CeO_2, we calculated the formation energies (FEs) of Os substituting Ce (Os_{Ce}) and Os_{Ce} accompanied by an oxygen vacancy ($Os_{Ce} + V_O$). The FE of Os_{Ce} on the CeO_2 (111) surface is 0.64 eV (Fig. S1), whereas that of $Os_{Ce} + V_O$ is −0.81 eV (Fig. 1a). The significantly lower FEs of $Os_{Ce} + V_O$ compared to Os_{Ce} indicate that oxygen vacancies form readily in Os-doped CeO_2. Compared to other investigated platinum-group metals, $Os_{Ce} + V_O$ exhibits the lowest FE, demonstrating the high structural stability of atomically dispersed Os in CeO_2 (Os_{SA}–CeO_2).

The strong anchoring of Os atoms originates from pronounced interfacial electronic coupling with the CeO_2 lattice, as revealed by DFT calculations. For metallic Os nanoparticles (Os_{NP}), the projected density of states (PDOS) displays delocalized Os 5d orbitals with occupied states at the Fermi level (Fig. 1b, left), showing metallic behavior. Upon Os doping into CeO_2, the 5d orbitals become localized, and unoccupied states above the Fermi level nearly vanish (Fig. 1b, right). This reflects charge redistribution and strong hybridization between Os and CeO_2. The modified electronic structure of Os in Os_{SA}–CeO_2 brings in different hydrogen adsorption behavior (Fig. 1c). The energy range of its hybridization with the H 1s orbital is approximately −6.3 to −2.3 eV for Os_{SA}–CeO_2 compared to −8 to −4 eV for Os_{NP}, indicating the weaker interaction between Os and H in Os_{SA}–CeO_2. The Gibbs free energy diagram for the HER (Fig. 1d) further supports this result. The calculated ΔG_{H^*} values for the Ce site in Os_{SA}–CeO_2 and Os site in Os_{NP} are −0.23 eV and −0.19 eV, respectively, implying facile H adsorption. However, this hinders the desorption of H*, thereby limiting the formation of H_2. In contrast, the Os site in Os_{SA}–CeO_2 exhibits a moderate ΔG_{H^*} of −0.08 eV and a shortened H–H

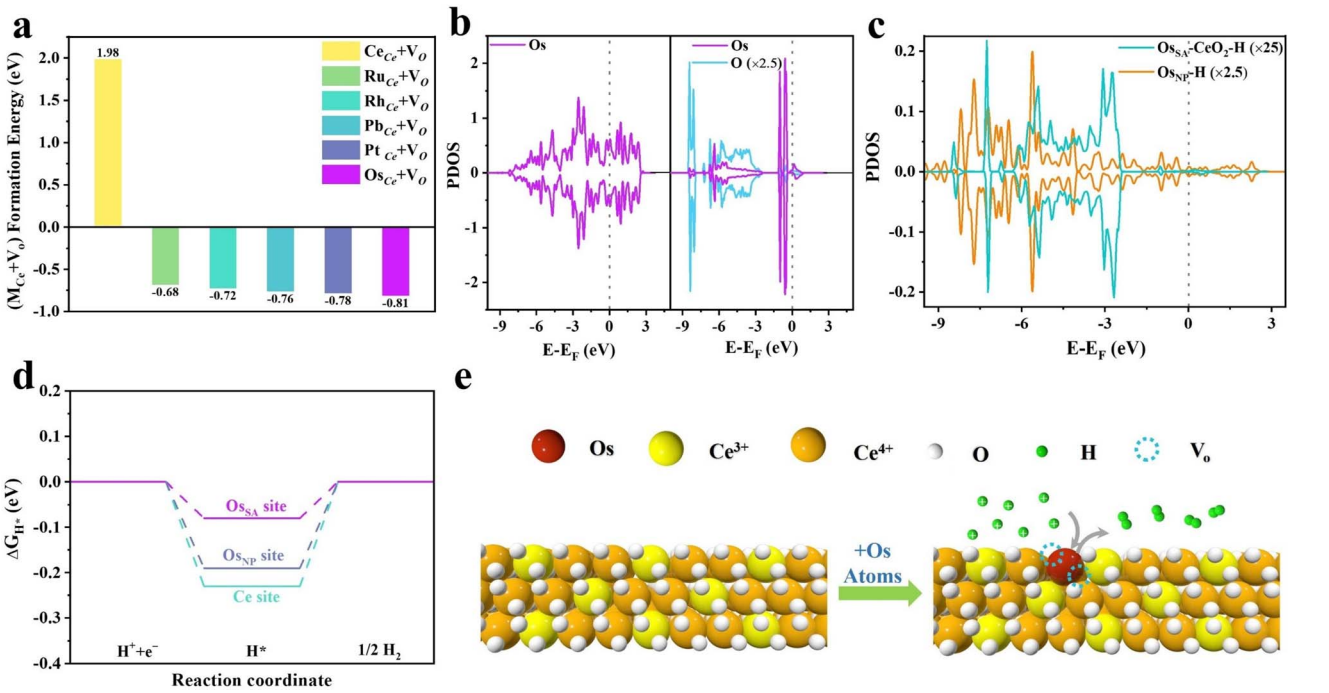

Fig. 1 Theoretical calculations illustrating the strong interfacial coupling of Os SAs in CeO_2. (a) Calculated formation energies of $M_{Ce} + V_O$ (M stands for the substituted atom for Ce). PDOS for (b) Os 5d orbital of Os_{NP} (left) and Os_{SA}–CeO_2 (right) and (c) H 1s orbital of adsorbed H. (d) Gibbs free energy diagram for the HER in acid media on Os_{NP} (blue line) and Os_{SA}–CeO_2 (purple and cyan lines). (e) Schematic mechanism of proton adsorption on the Os site leading to H_2 generation.

Open Access Article. Published on 22 1447. Downloaded on 10/12/47 07:47:25 .
This article is licensed under a Creative Commons Attribution 3.0 Unported Licence.

coupling distance (1.60 Å *vs.* 1.97 Å for Os_{NP}, Fig. S2), suggesting optimized hydrogen binding and improved HER kinetics. Overall, atomic Os incorporation into CeO_2 yields a stable configuration with balanced H* adsorption energy and robust structural anchoring (Fig. 1e).

Material synthesis and structural characterization

Guided by the theoretical predictions, we synthesized the Os_{SA}–CeO_2 sample consisting of Os SAs dispersed in the CeO_2 matrix (Fig. 2a). Compared with the dense film structure of CeO_2 (Fig. S3), the O_2 post-treatment induced CO_2 release from the carbon substrate, generating a porous structure of CeO_2–O_2 (Fig. S4) that was preserved in Os_{SA}–CeO_2 (Fig. 2b). The aberration-corrected high-angle annular dark field scanning transmission electron microscopy (HAADF-STEM) image (Fig. 2c) reveals abundant dark regions within the sheet-like aggregates, corresponding to the voids seen in the scanning electron microscopy (SEM) image (Fig. 2b). Elemental mapping (Fig. 2d

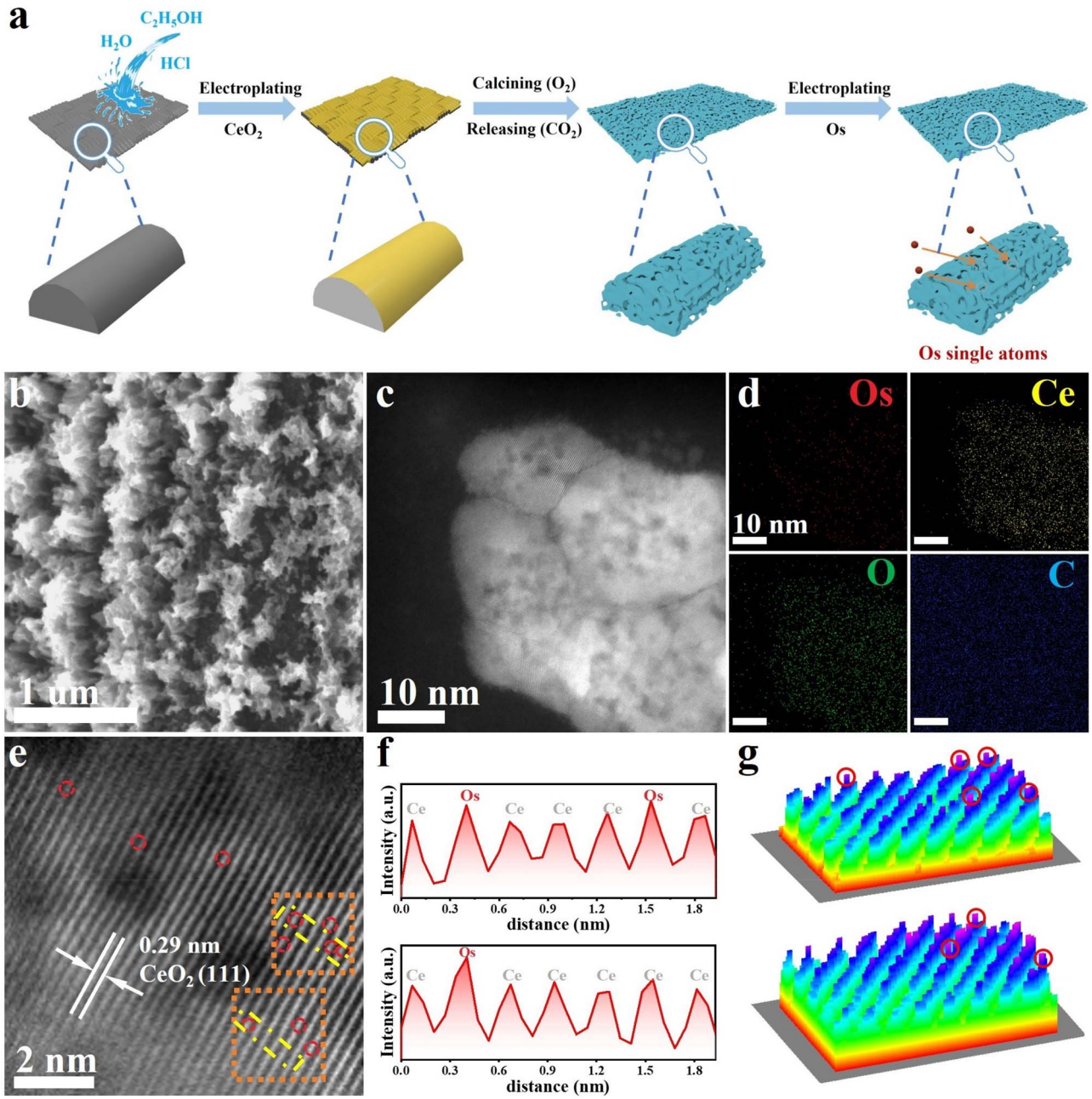

Fig. 2 Synthesis and morphological characterization of Os SAs anchored on porous CeO_2 (Os_{SA}–CeO_2). (a) Schematic illustration of the synthesis route for Os SAs dispersed on porous CeO_2. (b) SEM image of Os_{SA}–CeO_2. (c) HAADF-STEM image and (d) corresponding elemental mapping images of Os_{SA}–CeO_2. (e) High-resolution HAADF-STEM image of Os_{SA}–CeO_2. (f) Two-dimensional atomic distribution map corresponding to the yellow region highlighted in (e). (g) Three-dimensional atomic distribution map corresponding to the orange region highlighted in (e).

© 2026 The Author(s). Published by the Royal Society of Chemistry

Open Access Article. Published on 22 1447. Downloaded on 10/12/47 07:47:25 .
This article is licensed under a Creative Commons Attribution 3.0 Unported Licence.

and Table S1) and high-resolution STEM imaging (Fig. 2e) confirm the sheet-like CeO_2 structure with atomically dispersed Os. The reduced lattice spacing (0.29 nm *vs.* 0.31 nm for pristine CeO_2) indicates lattice compression due to Os incorporation. Fig. 2f shows the 2D atom distribution map of the yellow area framed in Fig. 2e. The atoms with higher intensity are Os single atoms, and those with weaker intensity are Ce atoms. The 3D atom distribution map of the orange area in Fig. 2e also demonstrates the successful preparation of Os single atoms.

Reference samples (Os_{NP}/CeO_2 and Os_{NP}) were prepared *via* the same electrodeposition route for Os (Fig. S5–S6). Compared to Os_{SA}–CeO_2, the electrodeposited CeO_2 film was annealed in Ar instead of O_2 in Os_{NP}/CeO_2, and the morphology remains flat for CeO_2–Ar (Fig. S7). For Os_{NP}, the carbon fiber without CeO_2 was directly used as the support for the deposition of Os. In contrast to Os_{SA}–CeO_2, Os aggregated into nanoparticles in both Os_{NP}/CeO_2 (Fig. S8) and Os_{NP} (Fig. S9). This indicates that the porous structure of the CeO_2 matrix is crucial for obtaining atomically dispersed Os atoms due to its much larger exposed surface area (Fig. S10). In addition, the Os loading amount is also necessary for the successful formation of Os single atoms (Fig. S11).

The electronic structure of Os in samples was investigated by X-ray photoelectron spectroscopy (XPS) and X-ray absorption near-edge structure (XANES) spectroscopy. In the Os 4f XPS spectra, the Os^{2+} fraction in Os_{NP}/CeO_2 is approximately 37 at%, which is a bit higher than the 36 at% for Os_{NP} (Fig. 3a). This is probably due to the electronic transfer between Os_{NP} and the CeO_2 support.[31,32] In contrast, Os_{SA}–CeO_2 exhibits a substantially increased Os^{2+} ratio of 46 at%. As revealed in Os L_3 edge XANES spectra, Os in Os_{SA}–CeO_2 possesses an oxidation state between those of metallic Os and OsO_2 (Fig. 3b). The much higher valence state of Os in Os_{SA}–CeO_2 further evidences the successful doping of Os into CeO_2 that enables strong electronic interactions between them. Also, the relatively lower valence of Os compared to Ce^{4+} will induce the generation of oxygen vacancies to keep the electronic balance,[34] consistent with the DFT results.

We studied the extended X-ray absorption fine structure (EXAFS) spectra to determine the coordination environments of Os in Os_{SA}–CeO_2. The Os L-edge R-space spectrum of Os_{SA}–CeO_2 (Fig. 3c) shows a dominant peak at ~1.72 Å corresponding to the Os–O band, and no peak of Os–Os bond is observed. The small peak at ~2.83 Å is probably ascribed to the Os–Ce bond,[24,35] as illustrated by the Fourier transform (FT) EXAFS fitting (Fig. S12 and Table S2). These verify the atomic dispersion of Os in CeO_2, consistent with the STEM results. Wavelet transform (WT)-EXAFS analysis (Fig. 3d and e) further confirms

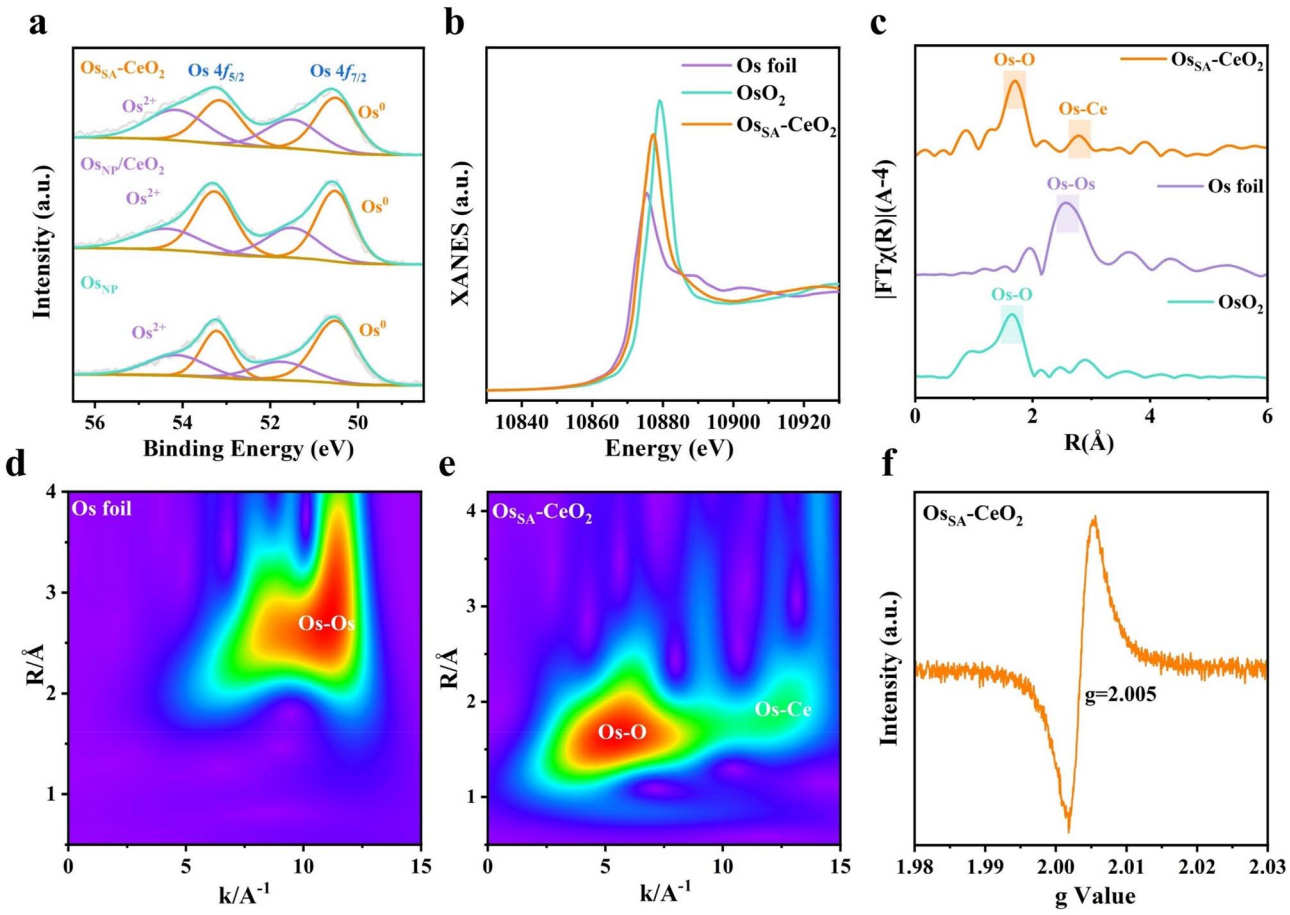

Fig. 3 Structural characterization of Os_{SA}–CeO_2. (a) High-resolution XPS spectra of Os 4f. (b) Os L_3-edge XANES spectra. (c) FT-EXAFS spectra of Os. WT of the k^4-weighted EXAFS spectra of (d) Os_{SA}–CeO_2 and (e) Os foil. (f) EPR of Os_{SA}–CeO_2.

Open Access Article. Published on 22 1447. Downloaded on 10/12/47 07:47:25 .
This article is licensed under a Creative Commons Attribution 3.0 Unported Licence.

the appearance of Os–O and Os–Ce bands in Os_{SA}–CeO_2. The Os–O coordination number (3.2, Table S2) is significantly lower than the Ce–O coordination (7.7) in CeO_2, indicating abundant oxygen vacancies, as confirmed by the electron paramagnetic resonance (EPR, Fig. 3f) and O 1s spectrum (Fig. S13) of Os_{SA}–CeO_2. The shorter Os–Ce bond (2.83 Å *vs.* Ce–Ce 3.30 Å) reflects lattice compression, consistent with the STEM results (Fig. 2e). Thus, we can conclude that the porous CeO_2 support enables the successful fabrication of atomically dispersed Os SAs, accompanied by the generation of numerous oxygen vacancies within the CeO_2 matrix.

Electrochemical performances

HER measurements were conducted in 0.5 M H_2SO_4 using a three-electrode setup. As shown in Fig. 4a, Os_{SA}–CeO_2 exhibits markedly superior HER activity compared to Os_{NP}/CeO_2 and Os_{NP}, approaching the performance of commercial 20% Pt/C.

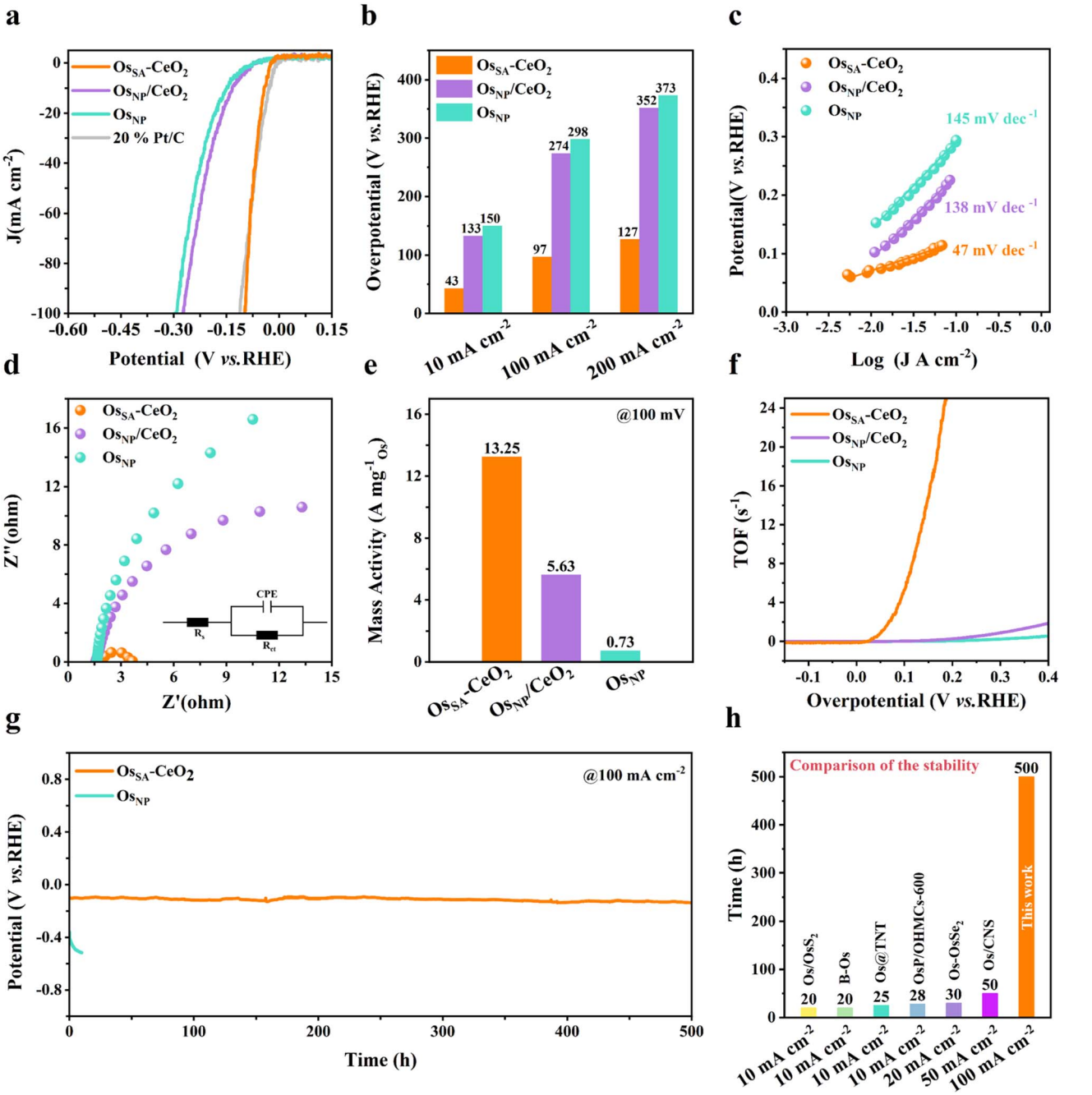

Fig. 4 HER performance of Os_{SA}–CeO_2 in acidic media. (a) HER polarization curves of various catalysts in 0.5 M H_2SO_4. (b) Comparison of overpotentials at 10, 100 and 200 mA^{-2}. (c) Tafel plots. (d) Nyquist plots; the inset shows the corresponding equivalent electrical circuit used for fitting. (e) Mass activity at an overpotential of 100 mV. (f) Relationship between TOF values and overpotentials. (g) Stability tests of Os_{SA}–CeO_2 and Os_{NP}. (h) Comparison of the stability of Os_{SA}–CeO_2 with previously reported Os-based HER catalysts in acidic media.[14,15,18–21]

© 2026 The Author(s). Published by the Royal Society of Chemistry

Open Access Article. Published on 22 1447. Downloaded on 10/12/47 07:47:25 .
This article is licensed under a Creative Commons Attribution 3.0 Unported Licence.

The overpotentials of Os_{SA}–CeO_2 are only 43 mV and 97 mV at current densities of 10 and 100 mA cm^{-2}, respectively (Fig. 4b). The Tafel slope (47 mV dec^{-1}, Fig. 4c) is significantly lower than that of Os_{NP}/CeO_2 (139 mV dec^{-1}) and Os_{NP} (145 mV dec^{-1}), indicating faster kinetics and a favorable HER pathway.[36–38] Electrochemical impedance spectroscopy (Fig. 4d) shows that Os_{SA}–CeO_2 possesses the lowest charge transfer resistance, as summarized in Table S3. These factors contribute to its exceptionally high mass activity (Fig. 4e) and TOF (Fig. 4f). The mass activity of Os_{SA}–CeO_2 is 13.25 A mg_{Os}^{-1} at 100 mV overpotential (Fig. 4e), 2.4 times higher than that of Os_{NP}/CeO_2 and 18.2 times higher than that of Os_{NP} (Table S4). The effect of Os loading on HER performance was further investigated by varying the deposition cycles (Fig. S14). Os-50 CV (Os_{SA}–CeO_2) exhibits markedly higher activity than Os-10 CV, while showing slightly lower activity than Os-90 CV. However, excessive Os loading in Os-90 CV leads to the formation of large aggregated nanoparticles (Fig. S11c), which is detrimental to achieving atomically dispersed active sites. Therefore, Os-50 CV, which balances high catalytic activity with atomic dispersion, was selected as the representative sample for further investigation.

Post-HER XPS analysis (Fig. S15) reveals minimal changes in Os binding energy for Os_{SA}–CeO_2, whereas Os_{NP}/CeO_2 and Os_{NP} exhibit positive shifts, indicating Os oxidation. Due to the strong interactions between Os and CeO_2 in Os_{SA}–CeO_2, the electron-buffering effect of CeO_2 regulates the electronic structure of Os and prevents its oxidation dissolution.[33,39] Controlled-current water electrolysis (Fig. 4g) was further done to test the long-term performance and stability. Os_{SA}–CeO_2 maintains stable operation for over 500 h at 100 mA cm^{-2}, far exceeding Os_{NP} and previously reported Os-based HER catalysts (Fig. 4h).

Insights into the origin of enhanced stability at large current densities

pH-dependent experiments (Fig. S16 and 5a) were performed to simulate the insufficient proton supply conditions that occur during high current operation. The overpotential at 100 mA cm^{-2} increases sharply with pH for Os_{NP} (slope = 171), indicating strong proton dependence, whereas Os_{SA}–CeO_2 shows a much smaller slope (16), suggesting additional water-splitting participation. Kinetic isotope effect (KIE) experiments (Fig. 5b) confirm this: HER performance in 0.5 M H_2SO_4 with D_2O is significantly lower than in 0.5 M H_2SO_4 with H_2O, due to slower D^+ migration and higher D–D bond energy, implying that H_2O dissociation contributes to H* generation on Os_{SA}–CeO_2. *Operando* infrared spectroscopy (Fig. 5c) further supports this

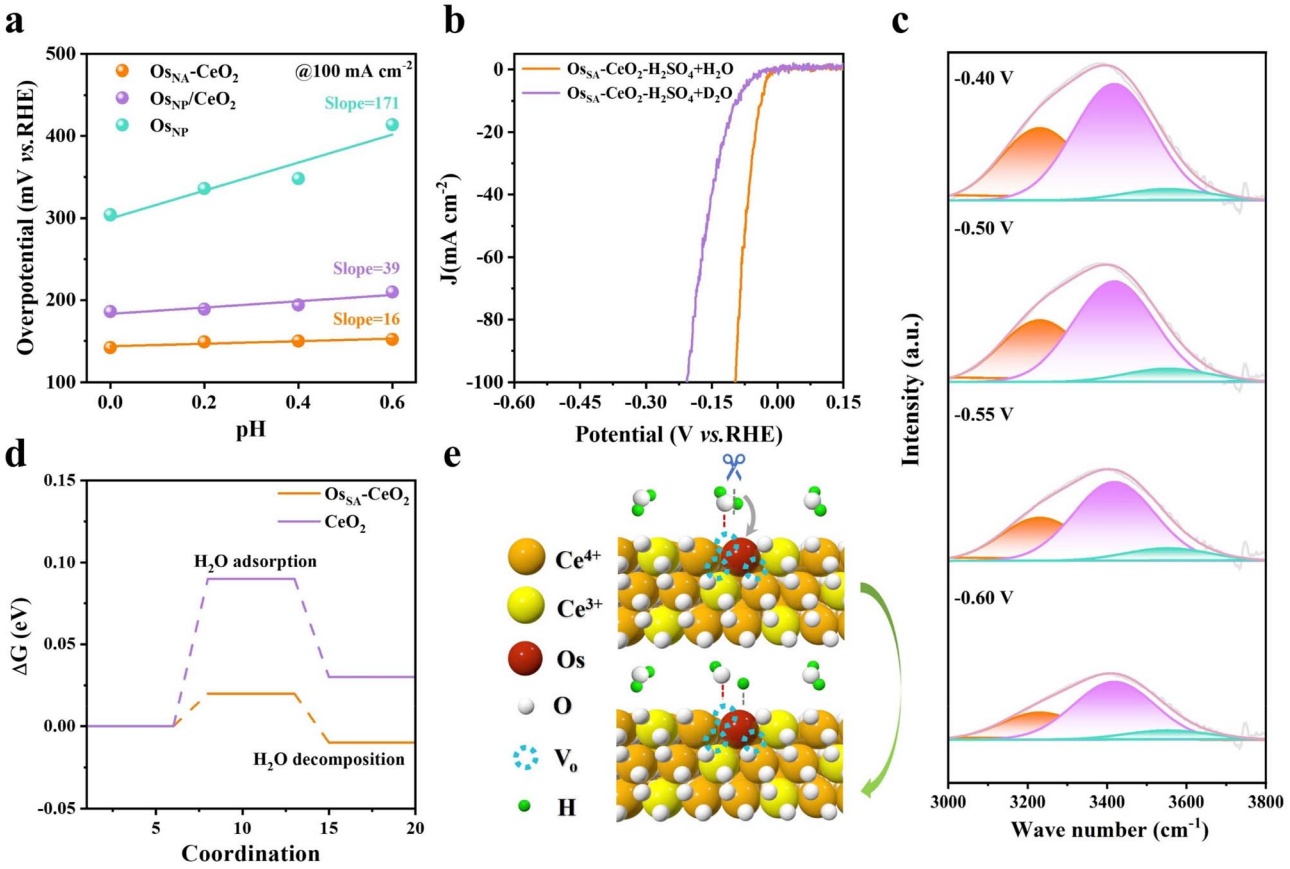

Fig. 5 Mechanistic insights into the H_2O splitting ability of Os_{SA}–CeO_2. (a) Overpotentials as a function of pH at100 mA cm^{-2} for Os_{SA}–CeO_2, Os_{NP}/CeO_2, and Os_{NP}. (b) LSV curves of Os_{SA}–CeO_2 measured in 0.5 M H_2SO_4 + H_2O and 0.5 M H_2SO_4 + D_2O. (c) *In situ* FTIR spectroscopy of Os_{SA}–CeO_2 at different applied potentials. (d) Gibbs free energy diagrams for H_2O adsorption and decomposition on Os_{SA}–CeO_2 and CeO_2. (e) Schematic illustration of the HER reaction pathway, showing H_2O as the supplied hydrogen source.

Open Access Article. Published on 22 1447. Downloaded on 10/12/47 07:47:25. This article is licensed under a Creative Commons Attribution 3.0 Unported Licence.

conclusion. The broad band from 3000–3800 cm^{-1} corresponds to interfacial water species, including 4-hydrogen bonding (HB)-H_2O (3231 cm^{-1}), 2-HB-H_2O (3418 cm^{-1}), and free H_2O (3553 cm^{-1}). With increasing negative potential, the proportion of strongly bound 4-HB-H_2O decreases, transforming into free H_2O (Table S5), indicating active water participation during the HER.[40]

The facile participation of H_2O for the HER on Os_{SA}–CeO_2 is probably due to the abundant oxygen vacancies. The oxygen vacancies can act as the strong adsorption sites for the oxygen-containing species like H_2O, which is confirmed by the DFT calculations (Fig. 5d). The Gibbs free energy barrier (ΔG) for H_2O adsorption decreases from 0.09 eV on CeO_2 to 0.02 eV on Os_{SA}–CeO_2, greatly facilitating H_2O dissociation. As summarized in Fig. 5e, Os doping induces oxygen vacancies that promote H_2O adsorption and splitting. The generated H* species migrate to adjacent Os sites, serving as a hydrogen source to support the rapid proton consumption at large current densities, thereby enabling stable HER operation. Also, the generated OH* species are adsorbed by the oxygen vacancies, thus preventing the Os sites from oxidative dissolution.

Conclusions

In summary, we have successfully synthesized an Os_{SA}–CeO_2 catalyst composed of atomically dispersed Os single atoms strongly anchored on a porous CeO_2 support. The porous CeO_2 architecture provides abundant anchoring sites that stabilize Os atoms and strengthen the Os–CeO_2 interfacial coupling. This interaction optimizes the electronic structure of Os, moderates H* binding strength, and induces abundant oxygen vacancies that activate CeO_2 toward enhanced H_2O dissociation. Benefiting from these synergistic effects, the Os_{SA}–CeO_2 catalyst exhibits outstanding HER activity in acidic electrolytes, surpassing commercial Pt/C at high current densities. It delivers a remarkable mass activity of 13.25 A mg^{-1} at 100 mV overpotential and maintains stable operation for over 500 h at 100 mA cm^{-2} with negligible degradation. This work provides a new design strategy to enhance the stability of noble-metal catalysts without sacrificing activity by engineering strong metal–support interfacial interactions.

Author contributions

J. Y. conceptualized the project. J. Y. and L. Z. supervised the work. Q. L. performed catalyst synthesis and general characterization. Q. L., M. L., W. L., and Y. H. contributed to experimental design and data analysis. Q. L. and J. Y. wrote the original manuscript draft. All authors contributed to discussions on the data and to the development of the manuscript.

Conflicts of interest

There are no conflicts to declare.

Data availability

The data supporting this article have been included as part of the supplementary information (SI). Supplementary information: experimental methods, additional DFT calculations, structure models for DFT calculations; SEM, TEM, schematic illustration of the synthesis route, EXAFS, XPS and ICP-OES; additional electrochemical data and summarized table for situ FTIR spectroscopy. See DOI: https://doi.org/10.1039/d5sc09741j.

Acknowledgements

This work was financially supported by the National Natural Science Foundation of China (no. 22472101), the Guangdong Science and Technology Department Program (2025A1515010431, 2024A1515011543, 2021QN02L252), the Shenzhen Science and Technology Programs (20231120181703001), the Research Team Cultivation Program of Shenzhen University (2023QNT007), and the Scientific Foundation for Youth Scholars of Shenzhen University (868000001032086). The authors sincerely acknowledge the Instrumental Analysis Center of Shenzhen University (Xili Campus) and Electron Microscope Center of Shenzhen University.

Notes and references

1 N. Johnson, M. Liebreich, D. M. Kammen, P. Ekins, R. McKenna and I. Staffell, *Nat. Rev. Clean Technol.*, 2025, **1**, 1–21.
2 M. Jin, J. Chen, X. Han, Y. Guo, Y. Liu, J. Wang, J. Li, Y. Yuan, H. Jin, S. Wang and X. Huang, *Nat. Commun.*, 2025, **16**, 11615.
3 Q. Zhang, Y. Dou, C. Liu, H. Fan, M. Cui, P. Liu, H. K. Liu, S. X. Dou and D. Yuan, *Electrochem. Energy Rev.*, 2025, **8**, 36.
4 Y. Guan, X. Yao, C. Xue, Z. Song, X. Ren, T. K. Sham, L. M. Liu, L. Zhang and X. Sun, *Adv. Funct. Mater.*, 2025, **35**, 202524427.
5 S. Riyajuddin, M. Pahuja, P. K. Sachdeva, K. Azmi, S. Kumar, M. Afshan, F. Ali, J. Sultana, T. Maruyama and C. Bera, *ACS Nano*, 2022, **16**, 4861–4875.
6 A. I. Feidenhans, Y. N. Regmi, C. Wei, D. Xia, J. Kibsgaard and L. A. King, *Chem. Rev.*, 2024, **124**, 5617–5667.
7 C. Hu, K. Yue, J. Han, X. Liu, L. Liu, Q. Liu, Q. Kong, C.-W. Pao, Z. Hu, K. Suenaga, D. Su, Q. Zhang, X. Wang, Y. Tan and X. Huang, *Sci. Adv.*, 2023, **9**, eadf9144.
8 M. F. Iqbal, M. Li, T. Xu, J. Yu, D. Xiong, Z. Mao, E. Hu, J. Zhang, P. Xu and Z. Chen, *Renewables*, 2024, **2**, 111–137.
9 G. Chen, J.-h. Zhang, K.-L. Zhou, Y. Yang, H. Ma, Y. Jin, J. Liu and H. Wang, *Front. Energy*, 2024, **18**, 369–377.
10 Y. Zhu, F. Guo, S. Zhang, Z. Wang, R. Chen, G. He, X. Sun and N. Cheng, *Electrochem. Energy Rev.*, 2025, **8**, 18.
11 J. Zhang, Z. Song, X. Yao, Y. Guan, Z. Huo, N. Chen, L. Zhang and X. Sun, *Chem*, 2025, **11**, 102498.

© 2026 The Author(s). Published by the Royal Society of Chemistry

Open Access Article. Published on 22 1447. Downloaded on 10/12/47 07:47:25. This article is licensed under a Creative Commons Attribution 3.0 Unported Licence.

12 Y. Guan, Z. Song, C. Xue, X. Yao, M. L. Zheng, J. Fu, W. Li, Y. Li, X. Ren, L. Zhang, L. M. Liu and X. Sun, *Adv. Energy Mater.*, 2024, **14**, 202402714.
13 M. Liao, T. Wu, Y. Zhong, Q. Lin, J. Qiu and L. Zhang, *Chem. Eng. J.*, 2025, **520**, 165284.
14 D. Cao, H. Xu, H. Li, C. Feng, J. Zeng and D. Cheng, *Nat. Commun.*, 2022, **13**, 5843.
15 Y. Li, C.-K. Peng, H. Hu, S.-Y. Chen, J.-H. Choi, Y.-G. Lin and J.-M. Lee, *Nat. Commun.*, 2022, **13**, 1143.
16 Y. Gao, Y. Xue, H. Wu, S. Chen, X. Zheng, C. Xing and Y. Li, *J. Am. Chem. Soc.*, 2024, **146**, 10573–10580.
17 D. Chen and S. Mu, *Energy Rev.*, 2023, **2**, 100053.
18 D. Chen, R. Lu, R. Yu, Y. Dai, H. Zhao, D. Wu, P. Wang, J. Zhu, Z. Pu, L. Chen, J. Yu and S. Mu, *Angew. Chem., Int. Ed.*, 2022, **61**, e202208642.
19 J. Zhu, F. Xia, Y. Guo, R. Lu, L. Gong, D. Chen, P. Wang, L. Chen, J. Yu, J. Wu and S. Mu, *ACS Catal.*, 2022, **12**, 13312–13320.
20 M. N. Krstajić Pajić, A. S. Dobrota, A. Mazare, S. Đurđić, I. Hwang, N. V. Skorodumova, D. Manojlovic, R. Vasilic, I. A. Pasti and P. Schmuki, *ACS Appl. Mater. Interfaces*, 2023, **15**, 31459–31469.
21 M. Liu, K. Shi, Z. Duan, M. Zhang, Y. Xu, Z. Wang, X. Li, L. Wang and H. Wang, *J. Mater. Chem. A*, 2022, **10**, 13042–13047.
22 L. Yang, S. Hou, S. Zhu, Z. Shi, X. Wang, J. Jiang, Y. Chu, J. Bai, Y. Wang, L. Zhang, Z. Jiang, C. Liu, W. Xing and J. Ge, *ACS Catal.*, 2022, **12**, 13523–13532.
23 F. Shen, Z. Zhang, Z. Wang, H. Ren, X. Liang, Z. Cai, S. Yang, G. Sun, Y. Cao, X. Yang, M. Hu, Z. Hao and K. Zhou, *Nat. Commun.*, 2024, **15**, 448.
24 J. Yu, J. Wang, X. Long, L. Chen, Q. Cao, J. Wang, C. Qiu, J. Lim and S. Yang, *Adv. Energy Mater.*, 2021, **11**, 2002731.
25 X. Liu, Y. Zhou, J. Lin, X. Xiao, Z. Wang, L. Jia, M. Li, K. Yang, J. Fan and W. Yang, *Angew. Chem.*, 2024, **136**, e202406650.
26 N. P. de Moraes, M. B. de Campos Sanmartin, R. da Silva Rocha, A. de Siervo, M. R. de Vasconcelos Lanza, D. A. Reddy, L. Yu and L. A. Rodrigues, *J. Rare Earths*, 2024, **42**, 314–322.
27 Y. Jiang, H. Fu, Z. Liang, Q. Zhang and Y. Du, *Chem. Soc. Rev.*, 2024, **53**, 714–763.
28 H. Liu, Q. Zhou, J. Yu, M. Nakabayashi, Y.-T. Lee, N. Shibata, Y. Li and J.-J. Delaunay, *ACS Catal.*, 2025, **15**, 8511–8521.
29 C.-H. Yan and X. Huang, *J. Rare Earths*, 2025, **43**, 2029–2052.
30 B. H. Yan, B. R. Xu, Y. Jin, H. Xiao, S. C. Luo, R. H. Duan, H. Li, X. Q. Yan, B. Lin and G. D. Yang, *cMat*, 2024, **1**, e28.
31 H. Liu, H. Duan, J. Yu, C. Qiu, R. Yu, J. Gao, S. Li, X. Du, Z. Si and S. Yang, *ACS Mater. Lett.*, 2022, **4**, 2572–2578.
32 H. Liu, J. Yu, J. Lin, B. Feng, M. Sun, C. Qiu, K. Qian, Z. Si, B. Huang and J.-J. Delaunay, *EES Catal.*, 2023, **1**, 720–729.
33 Y. Li, J. Zou, L. Sun, S. Liu, H. Li, Z. Song, J. Yu, L. Zhang and Z. Guo, *Adv. Funct. Mater.*, 2025, 2509899.
34 J. Yu, Q. Cao, Y. Li, X. Long, S. Yang, J. K. Clark, M. Nakabayashi, N. Shibata and J.-J. Delaunay, *ACS Catal.*, 2019, **9**, 1605–1611.
35 W. Tan, S. Xie, D. Le, W. Diao, M. Wang, K.-B. Low, D. Austin, S. Hong, F. Gao and L. Dong, *Nat. Commun.*, 2022, **13**, 7070.
36 W. Liang, Y. Zhang, D. Wang, J. Peng, J. Zou, H. Li, Z. Song, M. Tan, J. Yu and L. Zhang, *J. Phys. Chem. Lett.*, 2025, **16**, 12589–12595.
37 X. Zheng, X. Miao, Z. Yang, Z. Luo, J. Yu, H. Li and L. Zhang, *Chem. Sci.*, 2025, **16**, 19820–19829.
38 R. Wei, M. Liao, L. Sun, Q. Zhang, H. Zhang, L. Zhang and Z. Song, *ACS Appl. Mater. Interfaces*, 2024, **16**, 7141–7151.
39 Z. Dong, C. Zhou, W. Chen, F. Lin, H. Luo, Z. Sun, Q. Huang, R. Zeng, Y. Tan, Z. Xiao, H. Huang, K. Wang, M. Luo, F. Lv and S. Guo, *Adv. Funct. Mater.*, 2024, **34**, 2400809.
40 Y. Xu, J. Du, J. Jiang, Y. Miao, Z. Zhuang, Z. Liu, Y. Yan, R. Pan, J. Yang, M. Wang, S. Gu, L. Kang and D. Wang, *Angew. Chem., Int. Ed.*, 2025, **64**, e202502227.

© 2026 The Author(s). Published by the Royal Society of Chemistry